AGU PUBLICATIONS

JGR

Journal of Geophysical Research: Earth Surface

RESEARCH ARTICLE

10.1002/2015JF003641

Key Points:

- We quantitatively predict the sizes of icebergs from the properties of their icequakes
- Submarine ocean melt likely drives calving more rapidly during summer and fall than during winter
- Falling and low diurnal tides increase the rate of large iceberg calving events by >20%

Supporting Information:

- Data Set S1
- Data Set S2
- Data Set S3
- Data Set S4
- Figure S1 and Texts S1 and S2

Correspondence to:
T. C. Bartholomaus,
tbartholomaus@ig.utexas.edu

Citation:
Bartholomaus, T. C., C. F. Larsen, M. E. West, S. O'Neel, E. C. Pettit, and M. Truffer (2015), Tidal and seasonal variations in calving flux observed with passive seismology, *J. Geophys. Res. Earth Surf.*, *120*, 2318–2337, doi:10.1002/2015JF003641.

Received 12 JUN 2015
Accepted 18 OCT 2015
Accepted article online 22 OCT 2015
Published online 23 NOV 2015

Tidal and seasonal variations in calving flux observed with passive seismology

Timothy C. Bartholomaus[1,2], Christopher F. Larsen[2], Michael E. West[2], Shad O'Neel[3], Erin C. Pettit[4], and Martin Truffer[2]

[1]Institute for Geophysics, University of Texas at Austin, Austin, Texas, USA, [2]Geophysical Institute, University of Alaska Fairbanks, Fairbanks, Alaska, USA, [3]Alaska Science Center, U.S. Geological Survey, Anchorage, Alaska, USA, [4]Department of Geosciences, University of Alaska Fairbanks, Fairbanks, Alaska, USA

Abstract The seismic signatures of calving events, i.e., calving icequakes, offer an opportunity to examine calving variability with greater precision than is available with other methods. Here using observations from Yahtse Glacier, Alaska, we describe methods to detect, locate, and characterize calving icequakes. We combine these icequake records with a coincident, manually generated record of observed calving events to develop and validate a statistical model through which we can infer iceberg sizes from the properties of calving icequakes. We find that the icequake duration is the single most significant predictor of an iceberg's size. We then apply this model to 18 months of seismic recordings and find elevated iceberg calving flux during the summer and fall and a pronounced lull in calving during midwinter. Calving flux is sensitive to semidiurnal tidal stage. Large calving events are tens of percent more likely during falling and low tides than during rising and high tides, consistent with a view that deeper water has a stabilizing influence on glacier termini. Multiple factors affect the occurrence of mechanical fractures that ultimately lead to iceberg calving. At Yahtse Glacier, seismology allows us to demonstrate that variations in the rate of submarine melt are a dominant control on iceberg calving rates at seasonal timescales. On hourly to daily timescales, tidal modulation of the normal stress against the glacier terminus reveals the nonlinear glacier response to changes in the near-terminus stress field.

1. Introduction

Marine-terminating glaciers facilitate the most rapid rates of ice mass loss in Alaska, Greenland, and Antarctica [*Larsen et al.*, 2007; *Csatho et al.*, 2014; *Pritchard et al.*, 2012]. These glacier thinning rates, driven by tidewater glacier terminus retreat, can exceed global average thinning rates (largely driven by surface mass balance) by a factor of 10 or more [*Gardner et al.*, 2013; *Larsen et al.*, 2015]. While satellite remote sensing allows for the accurate quantification of total frontal ablation rates over weekly or longer timescales [e.g., *Rignot et al.*, 2011; *Burgess et al.*, 2013; *Enderlin et al.*, 2014], these timescales are insufficient to study the processes contributing to frontal ablation (calving and submarine melt) over the short timescales during which they occur and vary rapidly [*Walter et al.*, 2012; *Motyka et al.*, 2013]. Furthermore, the parsing of frontal ablation into its calving and submarine melt components is critical for the development of physical insight into changing tidewater glaciers. Attribution of mass loss to either calving or submarine melt allows for the development and testing of process-based models that can project future tidewater glacier mass change and sea level rise. This partitioning into calving and submarine melt remains a major challenge. Thus far, only labor-intensive and expensive oceanographic measurements can identify submarine melt rates from nonfloating termini [*Sutherland and Straneo*, 2012; *Bartholomaus et al.*, 2013; *Motyka et al.*, 2003], although passive hydroacoustics may represent an alternative approach [*Pettit et al.*, 2015]. Passive seismic methods have not yet quantified ice volume losses from mechanical iceberg calving processes [*O'Neel et al.*, 2010].

Wherever seismometers have been deployed in the vicinity of tidewater glaciers, transient seismic events ("icequakes") are observed in association with calving events [e.g., *Qamar*, 1988; *Amundson et al.*, 2010; *O'Neel et al.*, 2010; *Köhler et al.*, 2012; *Walter et al.*, 2012; *Veitch and Nettles*, 2012]. Calving icequakes are characterized by their detectability at ∼100 km distances, peaks in spectra between 1 and 5 Hz, emergent onsets lacking clear phase arrivals, and magnitudes typically below 2 [*Wolf and Davies*, 1986; *O'Neel et al.*, 2007, 2010; *Bartholomaus et al.*, 2012]. These calving icequakes contrast with another class of calving seismicity: the glacial earthquakes initially reported by *Ekström et al.* [2003]. Glacial earthquakes are characterized by their globally detected, 35–150 s period surface waves produced by seismic events that can exceed magnitude 5 [*Ekström et al.*, 2003; *Tsai and Ekström*, 2007; *Nettles and Ekström*, 2010]. In Greenland, these events predominantly originate at 15 of the largest outlet glaciers when full-glacier-thickness icebergs rotate and push off against the glacier terminus [*Amundson et al.*, 2008; *Tsai et al.*, 2008; *Veitch and Nettles*, 2012; *Murray et al.*, 2015]. Glacial earthquakes have not been identified in Alaska [*Nettles and Ekström*, 2010].

The different seismic character of glacial earthquakes and calving icequakes indicate that different source mechanisms are responsible for the two types of seismic events. However, calving icequakes do colocate with glacial earthquakes and occur both simultaneous with and independent of glacial earthquakes [*Amundson et al.*, 2010; *Walter et al.*, 2012]. Calving icequakes appear to be ubiquitous at the termini of calving glaciers.

This study builds on existing calving icequake research that has focused on the identification and location of calving events [*O'Neel et al.*, 2007, 2010; *Köhler et al.*, 2012]. Although iceberg sizes are potentially recoverable from glacial earthquake signals [*Tsai and Ekström*, 2007; *Veitch and Nettles*, 2012], few other studies have systematically demonstrated an ability to capture iceberg size, and therefore calving flux, using properties of calving icequakes. Notable exceptions have focused either on a small set of potential predictors [*Qamar*, 1988; *O'Neel et al.*, 2007] or on a short observation period [*Qamar*, 1988].

We focus here on Yahtse Glacier in southern Alaska, an advancing tidewater glacier and locus of regional calving icequake activity [*O'Neel et al.*, 2010]. While advancing at 100 m yr^{-1} [*McNabb and Hock*, 2014], thinning over the broad, upper glacier leads to overall mass loss [*Larsen et al.*, 2015]. Yahtse Glacier flows rapidly at its terminus (17 m d^{-1} in July 2011) where it meets sea water approximately 110 m deep in Icy Bay on the crest of an aggrading and prograding submarine moraine [*Bartholomaus et al.*, 2013]. Iceberg calving events at advancing Yahtse Glacier occur nearly once per minute [*Bartholomaus et al.*, 2012], several times more frequently than at nearby retreating glaciers [*O'Neel et al.*, 2003, 2007]. We have not observed, nor are we aware of, large, full-thickness calving events at Yahtse Glacier that occur over a substantial portion of the terminus width (such as those producing glacial earthquakes).

In this study, we present a quantitative model of iceberg size based on the properties of the icequakes they produce. Then we apply this statistical model to a set of 205,637 consistently detectable icequakes that we identify as produced by iceberg calving at Yahtse Glacier over 18 months. We interpret temporal variability in calving fluxes to infer the environmental factors controlling iceberg calving rates.

2. Data Sets

Our analysis of calving occurrence at Yahtse Glacier builds on a combination of locally recorded seismic data and a record of visually and audibly observed calving events. The seismic network included up to nine broadband seismometers buried within thin sediment near the terminus of Yahtse Glacier between June 2009 and September 2011 (Figure 1). The network aperture was approximately 12 km, and stations consisted predominantly of Guralp CMG-3Ts with Quanterra 330 digitizers and balers. These sensors have a flat response from 120 s to 50 Hz. Sampling rate varied over the course of our experiment between 100 and 200 samples per second [*Larsen and West*, 2009].

The observer record consists of direct visual or audible observations of 4589 events at the terminus of Yahtse Glacier over 12 days during June 2010 [described in *Bartholomaus et al.*, 2012]. Among other properties, the style of iceberg calving was recorded and the size of each calving event was estimated using an integer scale. "Size" is a semiquantitative estimate of iceberg volume and ranged from 1 to 7 based on the visual and audible impression of the calving event. Observers were trained to promote consistent size classifications; statistical analysis of the observer record reveals no bias in the estimated sizes (section 3.5). The occurrence rate of iceberg sizes is drawn from a power-law-like, right skewed distribution (we record 3329 size 1 icebergs for each size 7 iceberg). Calving styles consisted of audible-only events (AUD) either behind the glacier terminus or from an obscured portion of the terminus, loose avalanches of ice debris (AVY), subaerial drops (SAD) in which an intact iceberg drops straight down from the terminus, subaerial topples (SAT) in which an intact iceberg rotates out away from the terminus before impacting the water surface, and submarine-released (SM) icebergs rising from beneath the sea surface.

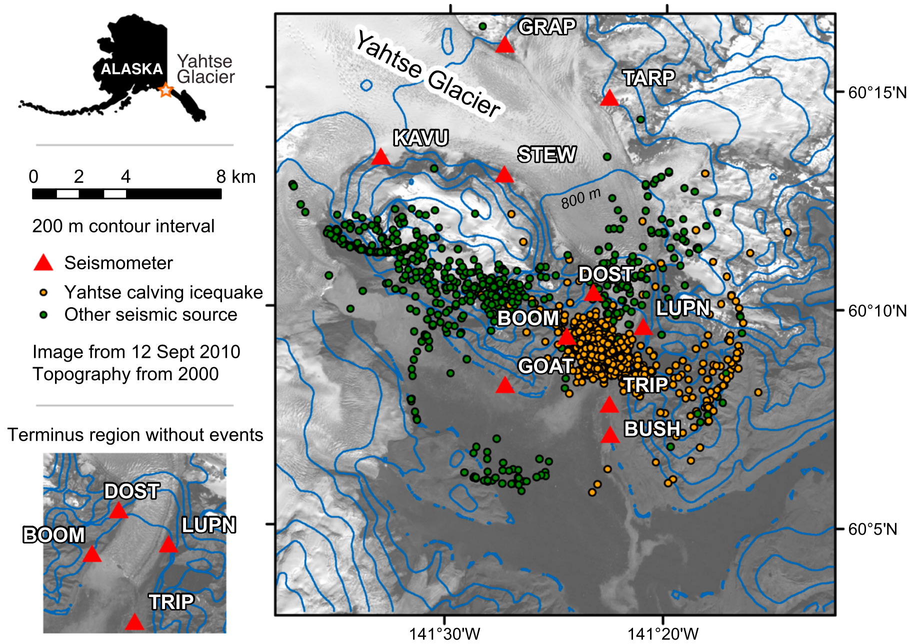

Figure 1. Map of lower Yahtse Glacier, with locations of icequakes and 10 seismic stations. Station TRIP was installed after station BUSH was damaged. Small orange and green circles identify the origins of 2000 seismic events identified as either produced by iceberg calving at Yahtse Glacier or produced by other processes. The terminus of Yahtse Glacier (shown at bottom left) is beneath the densest cluster of located Yahtse calving icequakes. The background image is a Landsat 7 scene overlain with contours from NASA's Shuttle Radar Topography Mission.

3. Analysis

To produce a time series of calving flux, our analytical procedure begins with icequake detection, then proceeds by locating icequakes at the Yahtse Glacier terminus, seismically characterizing each calving icequake, developing a statistical model relating icequake properties to iceberg size, and finally applying this model to the entire seismic record.

3.1. Seismic Event Detections

The seismic energy produced by calving icequakes at Yahtse Glacier and other tidewater glaciers in Alaska peaks between 1 and 5 Hz [*O'Neel et al.*, 2007, 2010; *Bartholomaus et al.*, 2012]. Therefore, we use the frequency domain detector described in *O'Neel et al.* [2007] to automatically detect all seismic events between 1 and 5 Hz recorded at the station BOOM, that closest to the Yahtse Glacier terminus. Data are processed in 1 h blocks, with 2 min of overlap between hours. We use a moving window fast Fourier transform on 2.5 s, 50% overlapping data segments. For each segment, we normalize the mean power in the 1–5 Hz band by the median power for each hour of data. An event is detected when the normalized power exceeds a signal-to-noise threshold of 10 and turns off when the normalized power falls back below 10. We use a penalty function analysis similar to that described in *O'Neel et al.* [2007] to determine the optimal parameter set for Yahtse Glacier. Detection times and durations on the station's vertical, northing, and easting channels are merged to create one master list of seismic detections while ensuring that individual seismic events are not counted twice. This yields a list of 568,911 detections during 606 days during which BOOM operated. The average detection rate was 0.65 events per minute; cumulatively, detections make up 13% of the operational time at BOOM.

3.2. Source Locations

Our goal is to cull the complete catalog of seismic detections to just those icequakes produced by calving at Yahtse Glacier. The first step is to remove tectonic earthquakes. Arrivals from teleseismic earthquakes are typically longer-period than the 1–5 Hz passband in which calving icequakes were detected at Yahtse Glacier and are unlikely to contaminate our catalog [*Bartholomaus et al.*, 2012; *Stein and Wysession*, 2003]. Arrivals from regional earthquakes do contain 1–5 Hz energy. Thus, we remove the 0.7% of detections that are potentially coincident with arrivals of seismic phases from earthquakes present within the catalog of the Alaska Earthquake Center ($M_L > 1.5$, available at http://www.aeic.alaska.edu/html_docs/monthly_reports.html).

Remaining detections may result from iceberg calving at Yahtse Glacier or one of the other tidewater glaciers in or near Icy Bay [*O'Neel et al.*, 2010; *Richardson et al.*, 2010; *Bartholomaus et al.*, 2012], other glaciological phenomena [e.g., *West et al.*, 2010], or landslides [e.g., *Zimmer et al.*, 2012].

The second step is to distinguish Yahtse Glacier calving events from other seismogenic phenomena. We locate the remaining detections using the decay of seismic amplitudes with distance [*Battaglia and Aki*, 2003; *Jones et al.*, 2013] and discard those distant from the Yahtse terminus. We expect icequake amplitudes to decay according to

$$A_{\mathrm{obs}}(r) = \frac{A_0}{r^n} e^{-\alpha r}, \tag{1}$$

where $A_{\mathrm{obs}}(r)$ is the maximum amplitude observed a distance r from the calving event, A_0 is the source amplitude, and n is 1/2 for surface wave spreading of seismic energy or 1 for body wave spreading. The exponential decay coefficient is $\alpha = \pi f / Q\beta$, for which f is the frequency of the seismic signals, Q is the quality factor for attenuation (large for materials with low anelasticity), and β is the seismic wave speed [*Battaglia and Aki*, 2003; *Jones et al.*, 2013]. To identify appropriate values for n and α, we fit equation (1) to a subset of icequakes produced by calving events witnessed at the terminus of Yahtse Glacier. $A_{\mathrm{obs}}(r)$ is the maximum amplitude of the Hilbert transformed waveform, filtered between 1 and 5 Hz, recorded at each of the stations within our network. We find that equation (1) is best fit with $n=1$ and $\alpha = 0.05$ km^{-1} and use these values for all locations going forward. With $f = 3$ Hz (a typical icequake frequency) and $\beta = 1.9$ km s^{-1} the speed at which the maximum amplitude signal moves through the network, $Q=100$.

Equation (1) is poorly suited to inversion-based location methods typically applied to identify earthquake epicenters using travel times. The $1/r^n$ term yields local minima in the error surface, in addition to the desired global minimum; these local minima are arrived at from some starting models. However, the simplicity of equation (1) makes it well suited to computationally efficient grid searches with which we can map the complete error surface surrounding our network. Therefore, our location algorithm applies equation (1) to each node of a rectangular grid covering the area of Figure 1 at 110 m spacing. The focal depth is set to 0 (i.e., icequakes are assumed to originate at sea level). We assign the origin of a given seismic event to the location where the error function

$$\mathrm{Err} = 100 \times \frac{\sum_{i=1}^{N} \left| A_{i,\mathrm{pre}} - A_{i,\mathrm{obs}} \right|}{\sum_{i=1}^{N} A_{i,\mathrm{obs}}} \tag{2}$$

is minimized (supporting information). In equation (2), N is the number of stations, $A_{i,\mathrm{pre}}$ is the amplitude predicted at station i using equation (1), and $A_{i,\mathrm{obs}}$ is the amplitude observed at station i. This differs slightly from the error function used by both *Battaglia and Aki* [2003] and *Jones et al.* [2013] in that we use the L_1 norm to minimize the impact of undesirable, local, seismic sources that may act as outliers, such as rockfall, wind noise, or calving at adjacent glaciers. The earlier authors used a L_2 norm version of equation (2) in their studies. For most seismic events, including those with the largest amplitudes, the form of the error function makes a small difference in the epicentral location; the difference between L_1 and L_2 norm locations for 93% of events is less than 2 km. For locations with larger L_1-L_2 distances, the L_1 norm more consistently located events at the glacier terminus when arrival times across our network were also consistent with a terminus origin.

After locating each of the potential icequakes, we manually examined the origins, error surfaces, and waveforms of 2000 arbitrarily selected seismic events during a time when our complete, nine-station network was operational. Waveform examinations considered whether the peak amplitudes used to locate the icequake at each station followed a consistent moveout from the predicted origin, whether the peak amplitudes were contaminated by other sources (Text S1 and Figure S1 in the supporting information), and whether the waveforms appeared similar to known Yahtse calving events [*Bartholomaus et al.*, 2012]. Based on these inspections, we identified each seismic event as the result of a Yahtse calving event or as generated by some other process (Figure 1). Of the 2000 seismic events, 1455 were consistent with a Yahtse calving source. We mapped each of the 2000 events and delineated a region in which nearly all of these Yahtse calving icequakes were located. Also present within this region were 30 (1.5%) false positives. Seismic events with sources distant from the Yahtse Glacier terminus (545 events) were also mostly identified correctly, with 515 located outside of the delineated region along with 28 (1.4%) Yahtse calving events (i.e., false negatives).

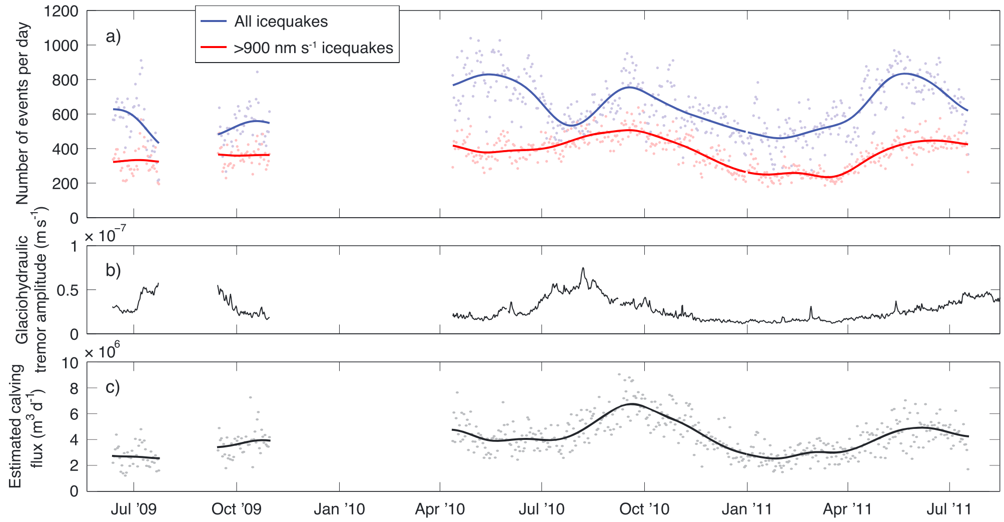

Figure 2. Icequake time series and derived calving flux at Yahtse Glacier. (a) The rate of all calving icequakes at Yahtse Glacier and the rate for that portion of larger-amplitude calving icequakes with peak amplitudes in excess of 900 nm s^{-1}, i.e., the "amplitude of completeness" (section 3.3). (b) The amplitude of glaciohydraulic tremor recorded at BOOM [*Bartholomaus et al.*, 2015]. (c) The estimated daily calving flux at Yahtse Glacier, produced using calving icequakes with peak amplitudes in excess of 900 nm s^{-1}. In Figures 2a and 2c, 2 month low pass filtered time series overlie the daily data.

To test the location algorithm's sensitivity to station dropout, we individually dropped stations from our location algorithm and reran the 2000 analyst-reviewed origin locations. We find that the algorithm is relatively insensitive to the specific network configuration, and mislocation errors remain small. In an extreme case, with only four stations operational (1 month in 2009), we can expect 5% false positives and 19% false negatives. The densest cluster of locations remains concentrated at the Yahtse Glacier terminus.

Based on this analysis, we use the automatic locations and delineated region to cull our detections and create a 348,267 icequake catalog of events produced by iceberg calving at the Yahtse Glacier terminus during the network's 18 operational months (Figure 2a).

3.3. Quantitative Icequake Properties

For each of these icequakes we extract 13 different seismic properties from the waveforms recorded on the vertical channel of BOOM (Figure 3). These are icequake duration (DUR, time of signal-to-noise threshold exceedance, section 3.1); maximum waveform amplitude (MAX); root-mean-square amplitude (RMS); pseudoenergy (ENR, the integral over time of the squared amplitude of the Hilbert transformed waveform); interdetection time since the last detection (TI1), 5 detections ago (TI5), and 20 detections ago (TI20); peak frequency of the icequake spectra (FREQ; >1 Hz to ensure we are not measuring microseisms); and five icequake envelope shape properties.

Visual observations paired with seismic data reveal that calving icequakes are produced by several-second-long, complicated, source processes [*Bartholomaus et al.*, 2012]. When convolved with Earth structure and instrument responses, long-duration icequake source-time functions lead to a wide variety of icequake shapes that generally lack the sharp *P* and *S* wave arrivals characteristic of most tectonic earthquakes [*Wolf and Davies*, 1986; *Stein and Wysession*, 2003]. To characterize diverse icequake shapes, we normalize the Hilbert transformed waveform (the waveform "envelope") in both time and amplitude and envision the transformed waveform as a probability density function (PDF) (Figure 3c). From this PDF-envisioned waveform, we calculate the first four moments: the mean (MEAN), standard deviation (STD), skewness (SKEW), and kurtosis (KURT; roughly "peakedness") of the amplitude, as well as the normalized time of maximum amplitude (MODE). *Köhler et al.* [2012] previously used waveform standard deviation, skewness, and duration, among other properties, to classify seismic events as either calving-generated or originating from some other process. Here we explore whether these properties can be used to further discriminate between larger and smaller calving events.

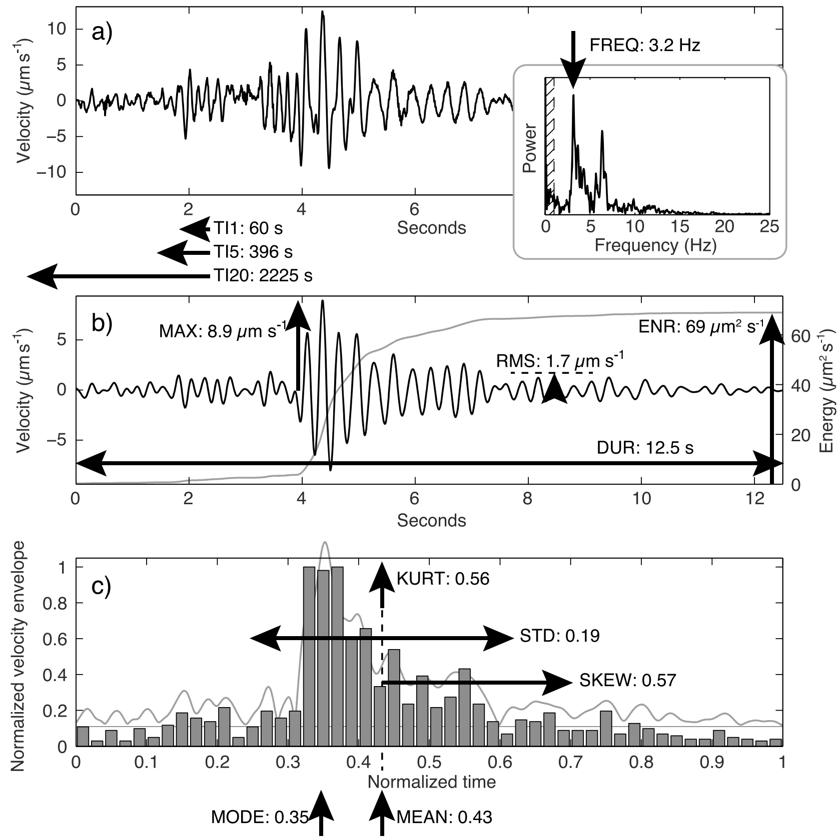

Figure 3. Illustration of the 13 icequake properties used to predict iceberg size labeled on a single, relatively simple icequake recorded at BOOM. (a) Unfiltered waveform. (b) Waveform filtered between 1 and 5 Hz and cumulative squared amplitude of the waveform envelope (gray), ENR. (c) Histogram derived from the Hilbert transform of the filtered waveform (the waveform envelope), plotted over the vertically offset Hilbert transform.

Our frequency domain detector identifies seismic events based on relative increases in power of the spectra between 1 and 5 Hz [*O'Neel et al.*, 2007]. All detectors, including ours, that use a fixed signal-to-noise detection threshold will detect fewer icequakes when the seismic noise floor rises. At Yahtse Glacier, background seismic noise increases during summer months (Figure 2b). This noise, produced by subglacial discharge and termed glaciohydraulic tremor, increases sharply during June of 2009 and 2010, reaches several local maxima in July and August, and decays toward background, winter levels in September [*Bartholomaus et al.*, 2015].

To limit the possibility of inconsistent detection capability, we examine a frequency-MAX plot of the icequakes located at Yahtse Glacier, similar in concept to a frequency-magnitude plot demonstrating the Gutenberg-Richter relation of earthquake occurrence (Figure 4) [*Gutenberg and Richter*, 1944]. On log-log axes, the icequakes with maximum amplitude between 900 and 10,000 nm s^{-1} lie along a straight line. The occurrence of icequakes with maximum amplitudes less than 900 nm s^{-1} fall below this straight line. The decrease in occurrence rate of small-amplitude icequakes is inconsistent with other aspects of iceberg calving, such as the sizes of icebergs, which have been shown to follow a scale-invariant, power law relationship [*Åström et al.*, 2014; *Chapuis and Tetzlaff*, 2014]. Therefore, we consider 900 nm s^{-1} to be the "amplitude of completeness" for our catalog (by analogy to a magnitude of completeness for earthquake catalogs [*D'Alessandro and Ruppert*, 2012]). We infer that we have detected every icequake with a maximum amplitude greater than 900 nm s^{-1}; however, our detector may not detect icequakes with lower MAX. At amplitudes higher than 10,000 nm s^{-1}, the number of icequakes is overpredicted by the straight line formed by lower amplitude icequakes. This may reflect an upper bound on icequake amplitude associated with the finite height of the glacier terminus.

In order to ensure that Yahtse Glacier calving icequakes are being detected consistently throughout the year, we discard those icequakes with MAX $<$ 900 nm s^{-1}, approximately 40% of our catalog. The occurrence rate of the remaining 205,637 larger-amplitude, Yahtse Glacier calving icequakes is shown in Figure 2a.

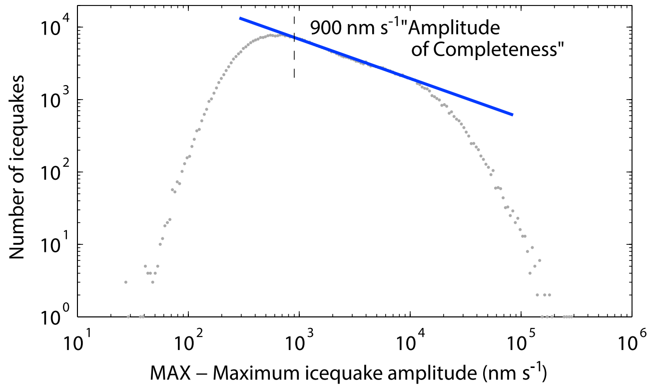

Figure 4. Frequency-maximum amplitude relationship for icequakes located at the terminus of Yahtse Glacier (binned logarthmically). Icequakes with moderate maximum amplitudes (MAX) lie along the blue straight line with log-log axes. Below 900 nm s^{-1}, the number of icequakes detected begins to deviate from this straight line.

3.4. Selection of a Statistical Model for the Prediction of Iceberg Size

Having identified the icequakes produced by iceberg calving at Yahtse Glacier, we seek to estimate the volumetric size of the seismogenic iceberg. We accomplish this by associating icequakes with known calving events from the June 2010 observer record that co-occur within 5 s of each other. Using the associated icequakes from this training period, we identify the most predictive statistical model of iceberg size using our 13 icequake properties. Our goals for model selection are prediction beyond the training period, physical insight into the importance and significance of the selected icequake properties, and model parsimony.

Icequakes originating from an observed calving event are included in the model training set if their maximum amplitude exceeds 900 nm s^{-1}. The icequake properties and corresponding iceberg sizes for 885 matched events are shown in each of the 13 panels of Figure 5. These boxplots allow us to identify which predictors vary systematically with iceberg size. We cannot be confident that the distributions of predictor values differ among size classes for properties FREQ, MEAN, SKEW, and TI20 ($\alpha = 0.05$ via the Kruskal-Wallis test). Furthermore, the relationships between iceberg size and STD, KURT, and TI1 are nonmonotonic, limiting their use as predictors of iceberg size. We remove these seven icequake properties from further consideration as regressors, leaving DUR, MAX, RMS, ENR, MODE, and TI5 as potential predictors of iceberg size. Additionally, we discard outlier events with properties more than three interquartile ranges from their medians; this yields a training data set of 794 events. Several of our regressors (DUR, MAX, RMS, and ENR) exhibit potential nonlinearities in their relationship with iceberg size (Figure 5). Square root transformation of these regressors is sufficient to linearize their relationships with the response variable [*Montgomery et al.*, 2001]. Thus, we allow for improvement in the linear relationship between iceberg size and DUR, MAX, RMS, and ENR by including in our model selection process the possibility that square-root-transformed versions of these icequake properties might be better predictors than their untransformed versions. We proceed with 10 candidate regressors: six original icequake properties and four square-root-transformed properties.

The sizes of iceberg calving events across all glaciers follow power law distributions [*Åström et al.*, 2014; *Chapuis and Tetzlaff*, 2014]. The sizes of our 794 observed and seismically detected calving events are similarly skewed. However, the challenge of consistently observing the smallest calving events, either seismically or in person, led to partial truncation of the smallest event sizes, with fewer size 1 events than size 2 events in our model training data set. For these data, the requirements of linear regression models with least squares estimates of model coefficients are not met; specifically, model errors are not normally distributed with constant variance. Thus, we predict iceberg size through the use of a generalized linear model (GLM), an alternate approach to estimating model coefficients that does not require these conditions on the data or residuals [*Montgomery et al.*, 2001; *Crawley*, 2009]. GLMs use a prescribed link function to fit the relationship between a set of regressors and a response variable whose expected values follow an exponential-family distribution. Residuals are examined to identify model inadequacies. We use a GLM with a log link and a gamma distribution for the response. Gamma distributions reproduce the skew of the training data set's observed calving events without predicting negative iceberg sizes. Other link functions and response distributions produce lower quality fits, as defined below.

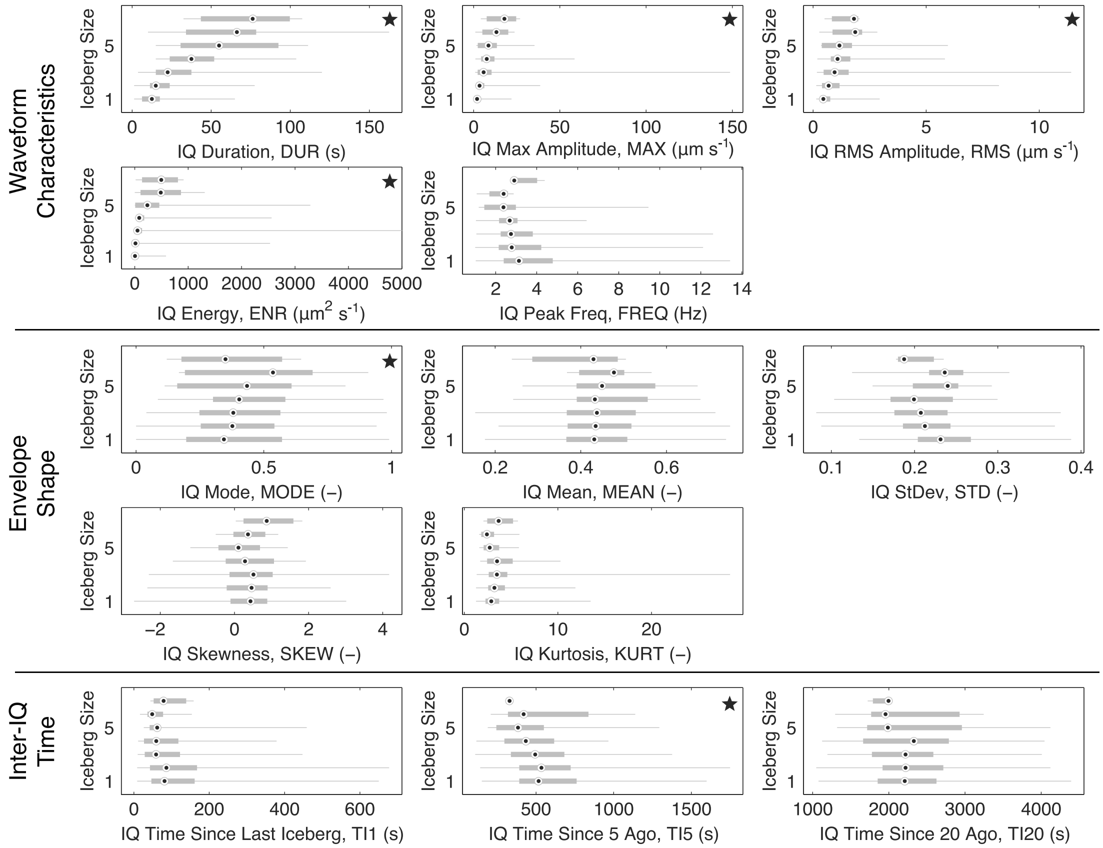

Figure 5. Boxplots showing relationships between icequake (IQ) properties and iceberg size for 885 observed calving events. The values for each iceberg size class of each icequake property are represented as horizontal boxes. The median property value for each size class is shown with the small bull's-eye. Wide gray bars extend across the interquartile range (IQR) from the 25th to the 75th percentile values. Thin lines span the remainder of the data. Stars mark six IQ properties included in the model selection process. Nonstarred properties exhibit no systematic relationship with iceberg size.

With 10 candidate regressors, we construct $2^{10} = 1024$ different models, where each model represents a different subset of the complete 10 regressor model. Because prediction beyond our training data set is our primary goal, we assess the performance of each of these 1024 models using fivefold cross validation [*Montgomery et al.*, 2001]. For each fold of each model, a random fifth of the observations are withheld for testing and coefficients are fit to the remaining four fifths of the observations. These coefficients are then applied to the withheld regressors, and we calculate the prediction root-mean-square error (RMSE) for the fold (where the error is the difference between the predicted and the observed responses). This process is repeated for each of the remaining four folds, then each model is ranked according to the mean RMSE of the five folds. However, the coefficients of the lowest RMSE model are not necessarily all significant, and multicollinearity among the regressors can lead to estimates of coefficients that are highly sensitive to small perturbations in icequake properties [*Montgomery et al.*, 2001]. Therefore, from the ranked models, we select the one with the lowest cross-validated RMSE for which we can, with 90% confidence, reject the hypothesis that one of the regressor coefficients is 0. We additionally require that all coefficients have a variance inflation factor <5. Multiple runs of these model selection steps ensure consistent arrival at a single best model.

The selected model includes the square root of icequake duration (DUR), the icequake root-mean-square amplitude (RMS), and the icequake mode (MODE) (Table 1). In addition to other statistics, we report the null and residual deviance. Deviance is a measure of misfit used in generalized linear models, where the null deviance is the deviance of a model fit with just a constant term, β_0, whereas the residual deviance is the deviance of the fitted model. A comparison between the observed and the modeled iceberg sizes is shown in Figure 6.

The p value for the duration coefficient is the lowest of the coefficients included in our model and the lowest among the 13 potential regressors in univariate regression; visually, the relationship between duration and

Table 1. Statistics for the Preferred Generalized Linear Model With a Gamma Error Distribution[a]: $\ln(\text{Size}) = \beta_0 + \beta_1 \text{DUR}^{1/2} + \beta_2 \text{RMS} + \beta_3 \text{MODE}$

Estimated Coefficients	Estimate	SE	*t* Statistic	*p* Value
β_0 (Intercept)	−0.052	0.046	−1.1	0.26
β_1 ($\text{DUR}^{1/2}$)	0.125	0.0099	13	$< 10^{-32}$
β_2 (RMS)	0.213	0.032	6.7	$< 10^{-10}$
β_3 (MODE)	0.181	0.064	2.8	0.0051

[a]SE is standard error of the coefficient estimate. Root-mean-square error of cross validation: 0.79; null deviance: 181; residual deviance: 121; *p* value for complete model: $< 1 \times 10^{-65}$.

iceberg size is more clear than any other relationship (Figure 5). Therefore, we also identify the univariate GLM for this most predictive, single-regressor model (Table 2). This model has only a slight loss in performance (cross-validation RMSE of 0.84) when compared with the preferred, three-regressor model (cross-validation RMSE of 0.79). Thus, a 5 s icequake is predicted to be generated by a size 1.5 iceberg, a 30 s icequake is produced by a size 2.4 iceberg, and a 90 s icequake is produced by a size 4.5 iceberg.

3.5. Converting Iceberg Size Classes to Volumes

During our observer period, we qualitatively estimated the sizes of calved icebergs by scaling them against the laser altimetry-surveyed, 60m height of the glacier terminus [*Johnson et al.*, 2013]. In-person observers were trained in the field to promote consistent size delineation. To identify potential observer bias in size estimates, we formed generalized linear mixed-effects models using methods nearly identical to those of section 3.4 but that include a random effect for the person recording calving activity in addition to fixed icequake property effects [*Bolker et al.*, 2008]. We found no differences in the sizes estimated by individual observers; thus, iceberg size classes are likely consistent and accurate to ±1 unit.

While in the field, we estimated the volume of icebergs for each of the seven classes. These estimates are well fit by

$$\text{Volume} \approx 700(\text{Size})^3 \qquad (\text{m}^3). \tag{3}$$

Uncertainties in our volume estimates lead to uncertainty in the particular form of this relationship, and we are unable to place quantitative confidence bounds on its coefficients. However, the third power is similar to

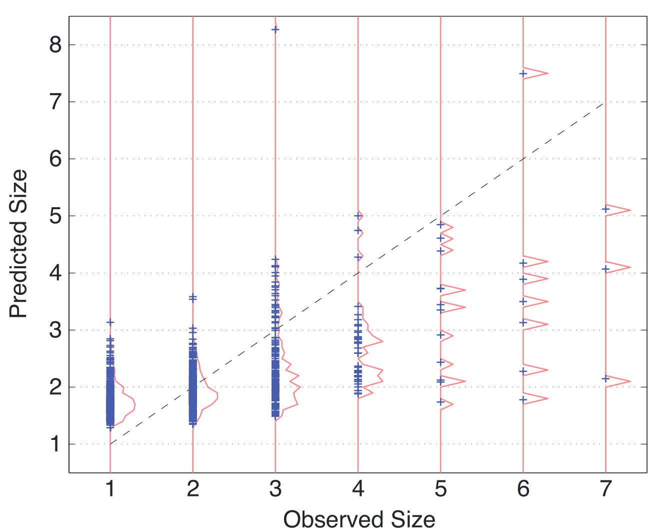

Figure 6. Observed and predicted iceberg sizes for each calving event in our training data set. The difference between these quantities are the model residuals. Plus symbols identify individual calving observations. Red lines represent empirical iceberg size density functions of the predicted sizes, so that the structure of the size distributions can be visualized when the iceberg/icequake observations plot on top of each other. The model overestimates the size of small (size 1) icebergs and underestimates the size of large icebergs (those greater than size 2). With a perfect model, observed and predicted sizes of each iceberg would be identical and all icebergs would fall on the dashed 1:1 line.

Table 2. Statistics for the Univariate (Dependent Only on DUR) Generalized Linear Model With a Gamma Error Distribution[a]: $\ln(\text{Size}) = \beta_0 + \beta_1 \text{DUR}^{1/2}$

Estimated Coefficients	Estimate	SE	*t* Statistic	*p* Value
β_0 (Intercept)	0.052	0.040	1.3	0.19
β_1 ($\text{DUR}^{1/2}$)	0.16	0.0092	17	$< 10^{-54}$

[a]SE is standard error of the coefficient estimate. Root-mean-square error of cross validation: 0.84; null deviance: 181; residual deviance: 129; *p* value for complete model: $<1 \times 10^{-58}$.

the exponent identified photogrammetrically by *Chapuis and Tetzlaff* [2014] and is consistent with our size estimates being a length scale. Plausible 50% variations in the scalar and exponent terms of equation (3) do not affect the conclusions we draw about calving variability.

3.6. Model Application to Complete Icequake Record

With an icequake-iceberg size model selected according to the training data set, we then apply it to the icequake properties of our complete 18 month record. Our model predicts a very small number of extremely large icebergs, well beyond the largest calving events observed in person (<0.1% of the number of Yahtse calving icequakes result in a predicted size > 9). Extremely large calving events, involving more than approximately 10% of the width of the glacier terminus, are also not apparent in time lapse photography of the glacier terminus. Spot checking of several of these extremely large-size events revealed that they result from long-duration detections in which multiple distinct icequakes occurring over several minutes are identified as a single detection. Thus, we remove these rare, inaccurately sized calving events from the record. Finally, we apply equation (3) to each estimated iceberg size, then sum each volume estimate by day to derive a time series of calving fluxes from Yahtse Glacier (Figures 2c and 7).

4. Discussion

4.1. Statistical Modeling of Calving Volume With Icequake Properties

4.1.1. Model Performance

Our preferred model (Table 1) predicts the range of observed iceberg sizes with a mean residual of 0 (Figure 6). The RMSE of predictions for which the observed iceberg size is known, but their associated icequake properties were not used in model fitting (i.e., cross validation), is 0.79 size units. This is similar to the precision of our qualitative iceberg size scale. The derived calving fluxes during our training period range between 2.4 and 5.4×10^6 m^3 d^{-1}, spanning from the 10th to the 82nd percentiles of our 2 years of calving fluxes. The coverage

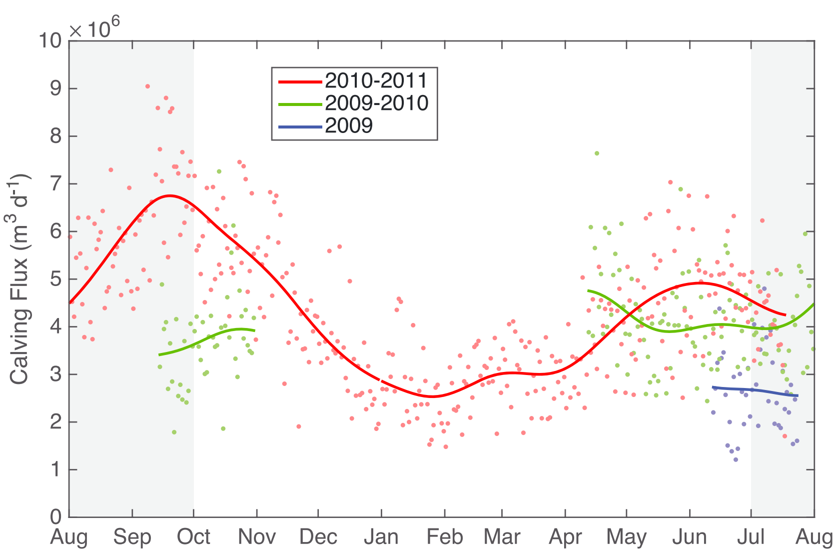

Figure 7. Daily calving flux derived from calving icequakes as in Figure 2, wrapped around 1 year to facilitate comparison among years. The choice of the 1 August break point is arbitrary. The July–September period during which glaciohydraulic tremor may lead to underestimated calving flux is shaded gray.

Table 3. Statistics for the Preferred Generalized Linear Model With a Gamma Error Distribution That Includes Calving STYLE[a]: $\ln(\text{Size}) = \beta_0 + \beta_1 \text{DUR}^{1/2} + \beta_2 \text{RMS} + \beta_3 \text{STYLE}$

Estimated Coefficients	Estimate	SE	t Statistic	p Value
β_0 (Intercept)	−0.103	0.073	−1.4	0.15
β_1 ($\text{DUR}^{1/2}$)	0.104	0.0094	11.1	$< 10^{-25}$
β_2 (RMS)	0.204	0.030	6.9	$< 10^{-10}$
β_3 (STYLE = AVY)	0	0		
β_3 (STYLE = AUD)	0.096	0.069	1.4	0.16
β_3 (STYLE = SAD)	0.197	0.066	3.0	0.0028
β_3 (STYLE = SAT)	0.492	0.090	5.5	$< 10^{-7}$
β_3 (STYLE = SM)	0.602	0.079	7.6	$< 10^{-13}$

[a]Coefficients for calving style use AVY as a reference category; thus, the coefficient estimates for AVY are 0. Root-mean-square error of cross validation: 0.75; null deviance: 181.07; residual deviance: 105.95; p value for complete model: $< 1 \times 10^{-86}$.

of these training data increases the likelihood that our model, tuned during 12 days in June 2010, is reliable across the full range of observed calving fluxes. Thus, our preferred model can be used to satisfactorily predict iceberg size from icequake properties.

However, the relationships between icequake properties and iceberg size are complex (Figure 5), and this complexity manifests in several model shortcomings. For example, the median duration for each iceberg size class increases with iceberg size, but large icebergs can also generate short icequakes and small icebergs can generate long icequakes. As a result of this data complexity, our preferred model overpredicts the sizes of small icebergs and underpredicts the sizes of large icebergs (Figure 6). Additionally, the number of size 1 icebergs is significantly underestimated. Because this stems from the underlying data used to build our model, this attribute is present in all empirical models that we tested. Other regressors, not identified in this study, may be required to significantly improve model fit, although inclusion of longer-duration, larger-sized calving events ($>10^6$ m^3, such as occur at retreating glaciers [*O'Neel et al.*, 2007; *Åström et al.*, 2014]) is likely to improve model performance.

Despite these limitations, the application of a statistical model for the estimation of iceberg sizes (and therefore calving fluxes) from icequake properties represents a significant improvement in our ability to observe iceberg calving, especially its variations. Not only do seismic methods allow for the consistent identification of calving, but our linear model constructed of statistically significant (p values < 0.1) icequake property regressors is also able to reliably predict iceberg size (RMSE <1 size unit).

4.1.2. Relationships Between Icequake Properties and Iceberg Calving Style

Iceberg calving style (e.g., loose avalanches or submarine releases) may also affect the connection between a calving event and the properties of calving icequakes, as *Bartholomaus et al.* [2012] previously suggested. With our training data set, we can include calving style as an additional categorical predictor of iceberg size and repeat our model selection steps (section 3.4). The result of this process is presented in Table 3. Both the transformed square root of icequake duration and the root-mean-square icequake amplitude reappear in this model, while icequake mode, with a comparatively high p value in Table 1, is replaced by STYLE in this most predictive model. Here STYLE acts as a modifier of the model's constant term, thus changing the predicted size for a given icequake (Figure 8b). For a moderately long-duration 60 s icequake, knowledge of calving style can make the difference between predicting a size 2.3 iceberg or a size 4.1 iceberg, equivalent to a nearly sixfold difference in predicted ice volume (equation (3)). Inclusion of calving style improves the predictive capability of a model (lowers cross-validated RMSE) and improves model fit (lowers residual deviance). For given durations, modeled iceberg sizes with STYLE (Table 3) better span the range of observed sizes than modeled iceberg sizes without STYLE (Table 1 and Figure 8).

Although submarine calving events are generally the longest-lasting, largest-sized calving events at Yahtse Glacier, Table 3 demonstrates that *for a fixed iceberg size*, icequakes produced by submarine calving events are expected to be of shorter duration and have smaller RMS amplitude than those produced by other calving styles. If a given icequake is known to be produced by an avalanche-style event, its predicted size will be significantly smaller than if it is known to be produced by a different calving style. In other words,

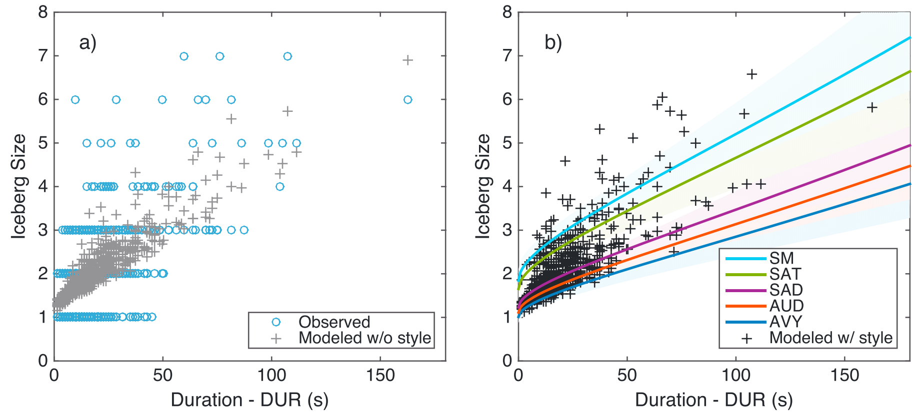

Figure 8. Iceberg size as a function of icequake duration, DUR, the most predictive regressor and calving style. (a) Observed sizes of calving events and their matched icequake durations and modeled iceberg sizes predicted using Table 1 and the same model training data. (b) Modeled iceberg sizes using the knowledge of calving style (Table 3). Crosses use the model training data in an attempt to replicate the observed data in Figure 8a. Solid lines are produced using synthetic data, including the median RMS value, a range of icequake durations, and the five calving styles; colored, transparent shadings span 95% confidence intervals of the iceberg size estimates. At iceberg sizes $\geq$ 3, not all calving styles are observed to occur. For example, only 2% of AVY events had size = 3 and no AVY events greater than 3 were observed during the 81h of calving observations.

submarine events are seismically the most subtle calving events, whereas avalanche calving events produce longer-duration, larger-amplitude calving events than would be expected given their size. Short-duration, low-amplitude icequakes produced even by large submarine calving events at Yahtse Glacier demonstrate that energetic interactions between icebergs and the sea surface produce the largest amplitude icequakes [*Bartholomaus et al.*, 2012]. Submarine calving events may detach from the terminus and rise to the surface too slowly to produce strong ground motion. However, at other glaciers, water depths greater than 100 m can allow icebergs to develop sufficient momentum to rise far above the water surface, thereby producing seismic energy subaerially when they collapse back to the sea surface [*O'Neel et al.*, 2007].

Toppling icebergs that rotate out and away from the terminus slap the water surface with broad faces. These calving events can produce impressive splashes on impact ("crown" splashes in hydrodynamics literature [e.g., *Truscott and Techet*, 2009]). However, their large seawater-contacting surface areas will produce commensurately large drag forces and toppled icebergs may not descend sufficiently below the water surface to produce the air cavities and Worthington jets that are responsible for the largest amplitude peaks in icequakes [*Bartholomaus et al.*, 2012]. Topple events, which by definition are composed of discrete and intact pieces of ice, may also unfold more quickly than comparably sized drops and avalanches. In contrast, avalanche-style calving events are produced entirely of cascades of loose ice debris—a relatively small calving event may produce a long-duration icequake.

These results illustrate that *how* icebergs calve and fall into the water is a first-order determinant of icequake generation [*Bartholomaus et al.*, 2012]. Our analysis at Yahtse Glacier is enabled in part by the relatively thin terminus, the high occurrence rate of iceberg calving, and the relative simplicity of calving at Yahtse Glacier—where full-glacier-thickness, multistage, overturning calving events are absent [cf., *Walter et al.*, 2012]. The present analysis additionally allows us to quantify the importance of calving style to icequake generation and better understand the processes by which icequakes are produced. Unfortunately, no method yet exists to automatically classify calving style and this data is generally unavailable (including during the majority of the 18 months of seismic observations at Yahtse Glacier). Thus, we are unable to include valuable information regarding calving style (Table 3) in our calculations of longer-term calving flux (Table 1 and Figure 7). Further analyses may reveal other icequake properties that can be used to predict calving style, or hydroacoustic methods may meet this need [*Glowacki et al.*, 2015]. Given the importance of calving style for icequake seismogenesis, we suggest that further research in this area be accompanied by investigations into the differences in and controls on calving style at tidewater glaciers. Application of the models presented here to glaciers with different typical calving styles may produce inaccurate results.

4.1.3. Relationships Between Icequake Properties and Iceberg Size

Our statistical model provides support for the findings of previous studies that found that icequake duration was a significant predictor of iceberg size and calving flux [*Qamar*, 1988; *O'Neel et al.*, 2007]. None of the icequake properties included in this study have more explanatory power than duration, although the square root of duration was a better fit to our observations than untransformed duration (Figure 5 and Tables 1 and 3). The relationship between iceberg size and duration is consistent with our observations in the field. The largest iceberg calving events evolve over long time periods. Smaller calving events tend to conclude quickly.

The icequake predictors that include waveform amplitude (MAX, RMS, and ENR) have moderate explanatory power and tend to increase with increasing iceberg size. However, their relationship with iceberg size is not nearly as strong as that of icequake duration. A single-regressor model with $DUR^{1/2}$ has a deviance 52 points lower than the null model (Table 2); further inclusion of RMS reduces the model deviance by another 7 points, and MODE affects an additional decrease of only about 1 point (Table 1). Furthermore, there may be some physical upper bound on icequake amplitude, such as the height from which an iceberg can fall (Figure 4), that would limit the relationship between icequake amplitude and iceberg size. These findings are similar to but more nuanced than other studies that found no clear relationship between icequake amplitude and iceberg size [*Qamar*, 1988; *O'Neel et al.*, 2007]. While iceberg size (and mass) affect icequake amplitude, over the range of calving events observed at Yahtse Glacier, the specifics of the icequake source mechanics appear to have a far greater impact on amplitude.

During model selection, we found that none of the three amplitude properties is clearly a stronger predictor than the others; MAX and ENR could be substituted for RMS with only a slight loss in predictive ability. Our efforts to reduce multicollinearity during the model selection process generally prevent more than one of these predictors from appearing together in the preferred model.

There is a positive, but weak, correlation between the relative time of the icequake peak amplitude (MODE) and iceberg size. The amplitude of size 1 icequakes most frequently peaks 1/3 of the way through the icequake's duration (MODE$=$ 0.33, Figure 5 and Table 1). As iceberg size increases, there is a tendency for the peak amplitude to shift toward the midpoint of the icequake (MODE$=$ 0.5). The tendency for MODE$<$ 0.5 with small iceberg sizes may be a product of the simply shaped icequakes produced by these small calving events. These simple icequakes have a single maximum in amplitude early during the icequake and a coda that is relatively long when compared with the total icequake duration. A consistent picture is revealed in the positive skewness of most icequakes (Figure 5; see Figure 3 for an example). The approach of MODE toward 0.5 with increasing iceberg size may reflect increasingly complex icequakes, with multiple peaks throughout the icequake duration, and a decreasing length of the icequake coda relative to the total icequake duration. However, we note that MODE and DUR are uncorrelated ($r = 0.09$), which increases the value of including both regressors, at least in Table 1.

The relationship between peak icequake frequency (FREQ) and size is weak. Regardless of the iceberg size, the median peak frequency is between 2.4 and 3.1 Hz. The IQR for each size class spans between 1.5 and 4.7 Hz. *Bartholomaus et al.* [2012] had previously suggested that icequake frequency should be negatively correlated with iceberg height and impacting surface area (i.e., iceberg size) and positively correlated with fall height. Figure 5 is suggestive of this relationship (a negative correlation between icequake frequency and iceberg size), but scatter within the present data prevent us from drawing any statistically significant conclusions. However, our findings do lend strong support to the use of dominant frequency in the attribution of icequakes to calving or other sources [*O'Neel et al.*, 2007; *West et al.*, 2010; *Köhler et al.*, 2012].

We also find weak, negative relationships between interevent time (TI1, TI5, and TI20) and iceberg size. Particularly for the elapsed time since five previous icequakes (TI5), large calving events are slightly more likely to occur following recent icequake activity than after periods of quiescence. This pattern is also supported by our field observations. Hours or days would pass with relatively little calving activity, then the calving rate would build to the eventual release of much larger icebergs [*Motyka*, 1997; *Bartholomaus et al.*, 2012]. This is consistent with a view of calving in which smaller cracks proliferate and connect under constant stress gradients, generating smaller calving events. These minor cracks eventually combine to form the runaway fracture that culminates in the calving of a large iceberg [*O'Neel et al.*, 2007; *Faillettaz et al.*, 2011; *Bassis and Jacobs*, 2013; *Åström et al.*, 2014]. However, the relationships between elapsed time and iceberg size do not contribute significantly to the most predictive models.

4.2. Variations in Calving Flux at Yahtse Glacier

The seismically derived calving flux varies at a range of timescales, along with the icequake occurrence rate. Over the 550 days for which we have daily calving fluxes and daily icequake occurrence rates, these quantities are correlated and the calving flux derived through our icequake statistical model can be predicted with the icequake occurrence rate,

$$Q = (1.3 \times 10^4)m - 5.6 \times 10^5, \tag{4}$$

in which Q is the calving flux (m^3 d^{-1}) and m is the number of icequakes per day exceeding our 900 nm s^{-1} amplitude of completeness ($R^2 = 0.68$, Figures 2a and 2c). In the sections that follow, we compare the mean seismically derived calving flux with previous estimates of frontal ablation and demonstrate how tides and seasonal submarine melt modulate the calving rate at Yahtse Glacier.

4.2.1. Mean Flux

During our observation period between June 2009 and July 2011, the estimated mean calving flux at Yahtse Glacier is 4.1×10^6 m^3 d^{-1}. Two prior estimates of the annually averaged sum of calving and submarine melt fluxes at Yahtse Glacier are 3.0×10^6 and 2.7×10^6 m^3 d^{-1} [*Burgess et al.*, 2013; *McNabb et al.*, 2015]. Our estimate of calving alone draws on only half the number of detected icequakes — those that can be detected reliably with a maximum amplitude > 900 nm s^{-1}. However, we expect that we have included nearly all of the largest-volume calving events.

In order to identify the calving and submarine melt contributions to total frontal ablation, we can use our seismically derived calving flux and knowledge of the ice flow speed and terminus width to estimate the thickness of ice lost to calving. Calving flux Q is equal to $w \times h \times u$, where w is the width of the terminus, h is the width-averaged thickness of the terminus lost to calving (not submarine melting), and u is the mean ice flow speed across the terminus. The terminus of Yahtse Glacier is 2.5 km wide, and ice speed near the center of the glacier terminus measures 17 m d^{-1} [*Bartholomaus et al.*, 2013]. Terminus-averaged speeds at fast-flowing Yahtse Glacier, 18 times wider than it is thick, may be up 10% lower than 17 m d^{-1} [*Cuffey and Paterson*, 2010]. Thus, we estimate that the glacier thickness involved in iceberg calving is between 95 and 110 m. Previous frontal ablation estimates, from regional studies, imply a terminus-averaged ice thickness of approximately 60–70 m [*Burgess et al.*, 2013; *McNabb et al.*, 2015].

The subaerial height of the Yahtse Glacier terminus has been measured at ~60 m [*Johnson et al.*, 2013]. Two lines of evidence suggest that the fjord at the glacier terminus is a maximum of 100–120 m deep. First, radar soundings of the lower terminus (approximately 100–200 m upglacier of the terminus and its submarine moraine) reveal that the centerline glacier bed is up to 150–200 m below sea level [*Rignot et al.*, 2013a, 2013b]. Second, extrapolation of centerline bathymetry indicates a depth of 110 m at the glacier terminus; the shape of the sounded fjord cross section indicates a mean depth of 80 m [*Bartholomaus et al.*, 2013] and a mean, width-averaged ice thickness of 140 m. A fjord floor slightly shallower than the glacier bed is consistent with the presence of a submarine terminal moraine, pushed in front of the advancing terminus. Thus, if 95–110 m of the 140 m thick terminal ice face is calved seismically, the remaining 30–45 m of submarine glacier thickness must be removed by small, undetected calving, submarine melt, or through submarine calving events whose sizes are underestimated (section 4.1.2). Analysis of Icy Bay oceanographic data supports a submarine melt hypothesis. *Bartholomaus et al.* [2013] found that melt by warm ocean water can remove more than half of the submarine ice flowing into the terminus.

4.2.2. Tidally Driven Variations in Calving Flux

Due to the limitations of our statistical model, we have higher confidence in the variability in our calving flux estimate than we do in the absolute magnitudes of the calculated calving flux. Around the mean rate of 4.1×10^6 m^3 d^{-1}, we find variability in the calving flux at a range of timescales. Gaps in the calving flux record prevent application of typical fast Fourier transform algorithms to quantify the strength of periodicity within the calving flux records. The Lomb-Scargle algorithm is an alternative for calculating power spectra that is well suited to irregularly spaced data [*Press et al.*, 1992]. Therefore, we sum our iceberg volumes within short-duration bins and present the Lomb-Scargle periodogram in Figure 9. We use an arbitrary bin size of 3.83 h to avoid aliasing the result with a bin size that is an even divisor of 24 h. Larger or smaller bin choices have only a small effect on the power or period of peaks.

We find a strong peak in the calving periodogram at 0.52 day, the same period as the principal lunar semidiurnal tide, M_2 (significant at $\alpha = 0.05$). Additional peaks are found at 1.0, 29.2, 32.6, and 39.8 days, although these do not clear the 95% confidence threshold. These are similar to or identical to the periods of the

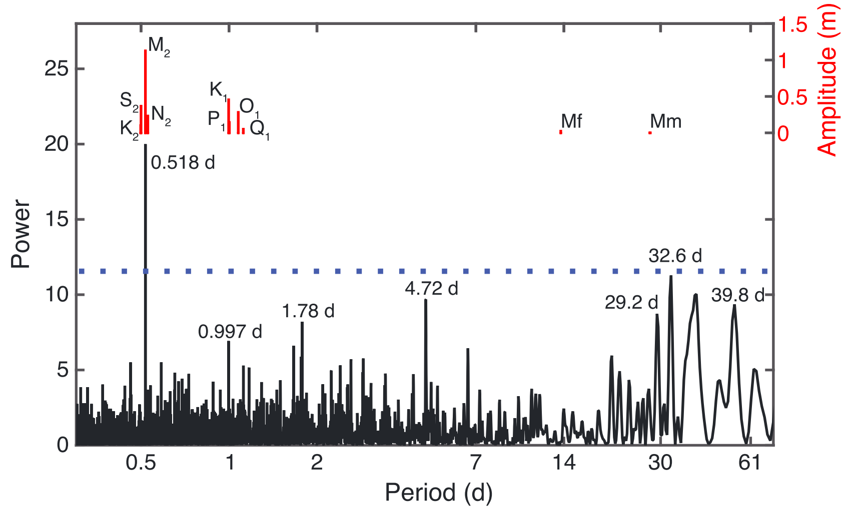

Figure 9. Power spectrum of iceberg calving flux calculated by applying the Lomb-Scargle algorithm to the demeaned, detrended calving flux in several-hour bins. The 95% confidence threshold that a peak is not drawn from a white noise spectrum is shown with dotted line. The periods of several peaks are labeled. The amplitudes of tidal constituents are shown in red.

following tidal constituents: principal lunisolar diurnal (K_1, 0.997 day), principal lunar diurnal (O_1, 1.08 days), and monthly (M_m, 27.6 days). The amplitudes of these constituents are also shown in Figure 9 (calculated for Yakutat, AK, 110 km ESE of Yahtse Glacier, http://tidesandcurrents.noaa.gov/harcon.html?id=9453220). The peaks at 1.78 and 4.72 days that do not coincide with tidal constituents are discussed in the next section.

To further explore the connection between ocean tides and calving activity, we calculate the seismically derived occurrence rate for differently sized icebergs during each high, falling, low, or rising tidal stage. We use a National Oceanic and Atmospheric Administration tidal model for upper Icy Bay (station 9453431 delayed by 30 min to match a tide gauge briefly installed at the Yahtse Glacier terminus during the 2010 summer). We consider high- and low-tide calving to be those events that occur within an hour of the semidiurnal maxima or minima. Otherwise, calving is classified as during rising or falling tides.

The strongly semidiurnal 2.9 m tidal range has a significant effect on the rate and size of calving events at Yahtse Glacier (Figure 10). For size 1 calving events, those with typical rectangular dimensions of 10 m on a side, tidal stage has a small effect, with calving ~6% more likely to occur during falling and low tides than during high tides. However, for increasingly large iceberg sizes, the tide has an increasingly large effect. For sizes 2, 3, 4, and 5 icebergs, the calving at low tides is 8, 16, 20, and 15% more frequent, respectively, than at high tides. The scarcity of large icebergs prevents robust calculation of mean rates for sizes larger than ~5; however, the relationship present within Figure 10 suggests that the effect of tides on calving rate may be even greater for the largest calving events.

Previous examinations of the influence of tides on iceberg calving have found mixed results. Fortnightly variability in calving has been found in some cases [*O'Neel et al.*, 2003] but not others [*O'Neel et al.*, 2010]. None of the studies reviewed have identified either semidiurnal or monthly calving variability [*Qamar*, 1988; *O'Neel et al.*, 2003, 2007, 2010]. *Warren et al.* [1995] described "weak" connections between tides and calving. In Greenland, studies to date have focused on the largest, approximately weekly, calving events that generate glacial earthquakes, to the exclusion of the more common smaller calving events that we describe in this study. Observation of significant power at the periods of multiple tidal constituents appears to be unique to this study.

We propose the following explanation. Yahtse Glacier terminates in water that is shallower than that of other well-studied glaciers, although the height of its terminus above sea level is comparable to that found at other glaciers [*O'Neel et al.*, 2003, 2007]. Thus, the normal stress at the bed of Yahtse Glacier is above average. The process by which tides modulate calving at Yahtse Glacier is unlikely to be through an increase in terminus buoyancy, at least not to the same degree as elsewhere. Instead, we propose that the normal stress applied by seawater against the near-vertical glacier terminus is the essential factor that sets the

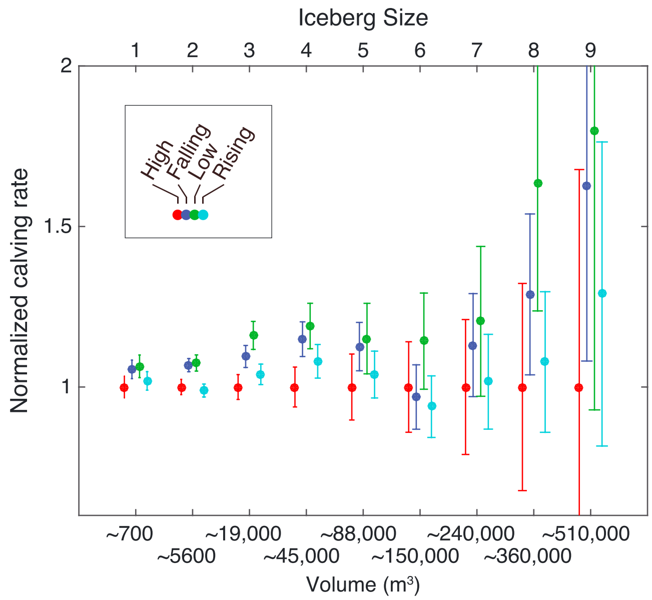

Figure 10. Variation in calving rate as a function of semidiurnal tidal stage for differently sized icebergs. For each of nine size classes, the mean calving rate is normalized by the mean rate of calving events during high tides. Volumes are estimated from equation (3). Bars extending from the means illustrate 95% confidence intervals.

calving sensitivity to tides. This is consistent with the observation that calving is enhanced during falling and low tides and with emerging research demonstrating that deep water inhibits, rather than accelerates, calving [cf. *Bassis and Walker*, 2012; *Brown et al.*, 1982]. For 110 m deep Icy Bay, the 2.9 m tidal range represents a variation in back pressure against the terminus face of ~3%. The up to 50% variation in calving rate for large icebergs in response to a 3% variation in forcing is the sort of nonlinearity that might be expected for a system that self-organizes to the critical point between stability and instability [*Åström et al.*, 2014]. In such systems, small environmental changes can lead to the calving of unpredictable ice volumes.

4.2.3. Nontidal, Multiday Variability

Also present within the calving periodogram (Figure 9) is weak 1.8 and 4.7 day periodicity, as well as other high-frequency variability. While the power of these peaks does not clear a 95% confidence threshold, they are present with little variation in their periods for all other calving flux bin sizes tested and even for other statistical relationships between icequake properties and iceberg size. We compared a version of the calving rate, high-pass filtered above a 0.083 d^{-1} cutoff frequency (12 day period) to daily rainfall, daily mean wind speed, and day-over-day mean temperature change, all recorded adjacent to the Yahtse Glacier terminus, as well as daily tidal range. These comparisons revealed a weak, negative relationship between rainfall and calving rate; however, this correlation might be due to the effect of glaciohydraulic tremor as described in the following section [*Bartholomaus et al.*, 2015]. The relationship weakens when the high-pass cutoff frequency is increased (for example, to a 4 day cutoff period). None of the other environmental variables explored correlate with the high-pass calving flux.

4.2.4. Calving Variability at Seasonal Periods

The seasonal view of calving flux variations demonstrates two time periods with above-average icequake-predicted calving (fall and spring) and two periods with below-average calving (summer and winter) (Figure 7). However, we have found that the summer decrease in calving flux is associated with a decrease in the estimated size of calving events [*Bartholomaus*, 2013]. These summer periods of decreased calving event sizes coincide with a summer increase in background seismic noise, attributed to subglacial discharge [*Bartholomaus et al.*, 2015]. The onset of glaciohydraulic tremor and the decrease in iceberg size are similarly abrupt. This leads us to suggest that the decrease in mean iceberg size is related to a decrease in the mean DUR of detected icequakes. While our amplitude threshold (Figure 4) provides some assurance that we detect icequakes consistently, glaciohydraulic tremor may decrease detected durations (i.e., the duration during which the amplitude of the seismic event rises above the detector's signal-to-noise threshold). Duration is the most important predictor of iceberg size (Table 1), so when DUR decreases, the predicted sizes follow suit.

Because we are not able to rule out the possibility that decreases in calving flux are due to the presence of glaciohydraulic tremor, we place low confidence in the estimated calving flux during these July–September time periods. These times are shaded light gray in Figure 7. We suggest that calving flux may peak earlier in the year than is shown in Figures 2 and 7, potentially during the July/August period when glaciohydraulic tremor is strongest. This may be supported by the slight increase in the occurrence rate of > 900 nm s^{-1} amplitude icequakes during July–September of 2010 (Figure 2a). Below, we interpret seasonal variations in calving flux in the absence of glaciohydraulic tremor, between October and June.

Outside of the July–September period, the clearest long-period pattern in calving flux is the 50% decrease in calving flux from December to March, during a time period with minimal seismic noise and excellent seismic station performance. Seasonal variations in terminus position are commonly observed in Alaska and Greenland [e.g., *Krimmel and Vaughn*, 1987; *Ritchie et al.*, 2008; *Howat et al.*, 2010; *Schild and Hamilton*, 2013; *McNabb and Hock*, 2014; *Stearns et al.*, 2015], with termini advancing through the winter and retreating during the summer. In Greenland, these variations have been attributed to decreased calving as a result of a backstress applied to the terminus by rigid ice mélange [*Amundson et al.*, 2010]. However, rigid mélange formation has not been observed at Yahtse Glacier and forms inconsistently at other Alaskan glaciers. The extent to which winter terminus advance in Alaska is the result of a decrease in calving or an increase in flow speed is not yet clear [*Stearns et al.*, 2015]. The winter minimum in iceberg calving that we report here suggests that at Yahtse, the decrease in calving flux is likely to be a major factor in the annual, 200–300 m winter advances of Yahtse Glacier [*McNabb and Hock*, 2014].

Previous studies of calving seismicity, including of the area surrounding Yahtse Glacier, have observed maxima during late August through October [*O'Neel et al.*, 2010; *Köhler et al.*, 2012]. The present results support these findings, particularly if we disregard the summer drops in calving flux (gray shading in Figure 7) or focus instead on the rate of large-amplitude icequake occurrence (Figure 2a). We propose that the fall increase in calving is driven in large part by rapid undercutting of the grounded terminus by submarine melt. Submarine melt is facilitated by both warm seawater and vigorous subglacial discharge [*Jenkins*, 2011; *Xu et al.*, 2012; *Motyka et al.*, 2013]. Both of these conditions are met on the Gulf of Alaska coast during the fall [*Bartholomaus et al.*, 2013]. Furthermore, the terminus is at an extended summer position, perhaps somewhat beyond the submarine moraine against which Yahtse Glacier presently terminates [*Bartholomaus et al.*, 2012].

In light of rapid submarine melt and an exposed terminus position, we find that the fall increase in iceberg calving that we and previous authors report can be explained by undercutting of the terminus and collapse of unstable, subaerial seracs. At this seasonal timescale, our hypothesis contrasts with previous studies that have suggested calving is dominantly controlled by longitudinal tensile stresses near the terminus [*Benn et al.*, 2007; *Cook et al.*, 2012; *Bassis and Walker*, 2012]. At both advancing and retreating grounded tidewater glaciers, measured longitudinal strain rates can be compressional within several kilometers of the terminus [*O'Neel et al.*, 2005; *Stearns et al.*, 2015], in contradiction to this "calving law." Instead, we suggest that the winter minimum in calving follows from minimum rates of submarine melt [*Bartholomaus et al.*, 2013] and, at Yahtse Glacier, a seasonally retracted terminus position perhaps protected from warm water by a submarine terminal moraine [*Motyka and Truffer*, 2007]. Melt-driven calving may also explain the observed seasonality in calving rates at Columbia Glacier [*van der Veen*, 2002]. There the seasonal cycle of calving (implicitly including submarine melt) is nearly identical to the seasonal cycle of submarine melt rates postulated by *Bartholomaus et al.* [2013]. We cannot evaluate the possibility that tidewater glacier dynamics, including seasonal variations in near-terminus speed [*Stearns et al.*, 2015], may at least partially control the rate of iceberg calving at some glaciers. However, we find that submarine melt, forced by seasonally varying water temperatures and subglacial discharges [*Jenkins*, 2011; *Xu et al.*, 2012; *Sciascia et al.*, 2013; *Bartholomaus et al.*, 2013], can explain seasonally varying calving at Alaskan glaciers without additional consideration of tidewater glacier dynamics.

5. Conclusions

Glaciologists and seismologists are increasingly applying passive seismic methods to glaciers due to the methods' ability to resolve short-duration events that are undetectable using other techniques. Iceberg calving has been a particular focus [e.g., *Qamar*, 1988; *Ekström et al.*, 2003; *O'Neel et al.*, 2007, 2010; *Köhler et al.*, 2012; *Amundson et al.*, 2010; *Walter et al.*, 2012; *Veitch and Nettles*, 2012]. However, previous attempts to tie calving seismicity to glacier dynamics have been stymied by an inability to quantitatively tie icequakes to iceberg volumes [*O'Neel et al.*, 2010; *Walter et al.*, 2012]. Without this relationship, rates of mass loss from calving cannot be inferred. In this study, we have identified an empirical relationship at Yahtse Glacier between icequake properties and iceberg size and used it to derive an 18 month time series of calving flux. Our method reveals several previously unknown patterns that improve our understanding of iceberg calving, including a midwinter minimum in iceberg calving and a strong calving response to low and falling semidiurnal tides. We also confirm the presence of rapid autumn calving at Yahtse Glacier and partition calving and submarine melt ice losses consistent with *Bartholomaus et al.* [2013].

We applied and validated an icequake locating algorithm to a data set with several hundred thousand events at Yahtse Glacier. After non-Yahtse calving icequakes were discarded, our final data set included 205,637 calving icequakes with sufficient amplitudes that we could be confident in our ability to detect them consistently throughout the year. In developing a generalized linear model for iceberg size, we explored the relationships between 13 different icequake properties and iceberg size. Icequake duration (DUR or its square root) is the single best predictor of iceberg size. Waveform amplitude-based metrics (MAX, RMS, and ENR) provided some explanatory power. Peak frequency (FREQ) and most icequake shape properties (MEAN, STD, SKEW, and KURT) did not conclusively vary with iceberg size. The style by which a calving event occurs affects predicted calving size to an extent comparable to the icequake duration. Per unit volume of ice, we find that avalanching-style calving events produce icequakes with greater amplitudes and longer durations than submarine-released icebergs (Table 3). This finding strengthens the previous conclusion of *Bartholomaus et al.* [2012]: that the interactions between icebergs and the fjord surface are paramount in producing calving icequakes.

Our study also illustrates the utility of in-person observations of iceberg calving (as also shown by *Qamar*, 1988; *O'Neel et al.*, 2007]. Our observer record allowed us to link icequake properties with known calving events, then use this validated relation to extend the calving record beyond the time of the observer record. We expect that the general features of our statistical model may well be universal—for example, our study supports the previously identified relationship between icequake duration and iceberg size [*Qamar*, 1988; *O'Neel et al.*, 2007]. However, the coefficients within Table 1 may vary from site to site as the terminus-station distance and the iceberg calving style change. Icequake flux estimates for different glaciers will be improved by local calibration. Glaciers calving into deeper water, or with less pervasively fractured termini than Yahtse Glacier, could potentially have different icequake signatures. New statistical approaches and machine learning that use large sample sizes to maximum advantage are likely to yield further insight. However, if the icequake occurrence rate/calving flux relationship (equation (4)) holds at different sites, networks of relatively inexpensive short-period seismometers or geophones may be sufficient for the counting of icequakes and estimation of iceberg calving fluxes [*Köhler et al.*, 2012].

In this study, we have demonstrated how icequakes can be used to remotely, automatically track rates of iceberg calving at a single glacier. High-rate continuous sampling makes seismology particularly well suited to observing calving over the seconds during which calving occurs. Provided that our method is tuned for a broad suite of glaciers, preexisting networks of seismometers can be used to track the temporal evolution of iceberg calving across entire mountain ranges and ice sheet margins. As we have found through application at Yahtse Glacier, seismic tracking of calving improves our knowledge of the environmental factors that modulate calving rates. Tidal variations in normal stress against the glacier terminus alter the calving rate on hourly to daily timescales, whereas submarine melt rates modulate the calving rate at seasonal timescales. Other factors, such as surface mass balance and glacier geometry, might be leading controls on calving rates at still longer timescales [*Enderlin et al.*, 2013; *Carr et al.*, 2015]. This new understanding of the rapidly changing dynamics of ocean-terminating glaciers can serve as a target for theoretical improvements in calving laws and their implementation in ice flow models.

Acknowledgments
This study was made possible by the National Science Foundation, through grant EAR-0810313. Additional funding is from the University of Texas Institute for Geophysics, USGS Climate and Land Use Change Program, and Department of the Interior Climate Science Center. We gratefully acknowledge the dedication of our expert pilots, Tony Oney and Paul Claus, who contributed significantly to the success of this project. We acknowledge the loan of seismic equipment and field assistance from PASSCAL Polar Programs. UNAVCO provided geodetic instruments for our experiment. Seismic data used here are available through the IRIS Data Management Center (network XF, YAHTSE, [*Larsen*, 2009]). Additional data sets, including the complete observer record of calving events, the matched observer and seismic observations of calving events, and the 18month record of individual calving icequakes are available as supporting information data sets. We thank Sophie Gilbert for suggestions regarding statistical approaches. We thank David Conner and Jared Steyaert for their meticulous help with the calving observer record. The Wrangell Mountains Center, McCarthy, AK, provided logistical assistance. Waveform figures and analyses were prepared with the GISMO toolbox [*Reyes and West*, 2011]. We thank Martin O'Leary, an anonymous reviewer, and Editor Bryn Hubbard for comments that improved the clarity and precision of our manuscript.

References

Åström, J. A., et al. (2014), Termini of calving glaciers as self-organized critical systems, *Nat. Geosci.*, *7*(12), 874–878, doi:10.1038/NGEO2290.

Amundson, J. M., M. Truffer, M. P. Lüthi, M. Fahnestock, M. West, and R. J. Motyka (2008), Glacier, fjord, and seismic response to recent large calving events, Jakobshavn Isbræ, Greenland, *Geophys. Res. Lett.*, *35*, L22501, doi:10.1029/2008GL035281.

Amundson, J. M., M. Fahnestock, M. Truffer, J. Brown, M. P. Lüthi, and R. J. Motyka (2010), Ice mélange dynamics and implications for terminus stability, Jakobshavn Isbræ, Greenland, *J. Geophys. Res.*, *115*, F01005, doi:10.1029/2009JF001405.

Bartholomaus, T. C. (2013), Seismicity, seawater and seasonality: New insights into iceberg calving from Yahtse Glacier, Alaska, PhD dissertation, Univ. of Alaska Fairbanks, Alaska.

Bartholomaus, T. C., C. F. Larsen, S. O'Neel, and M. E. West (2012), Calving seismicity from iceberg-sea surface interactions, *J. Geophys. Res.*, *117*, F04029, doi:10.1029/2012JF002513.

Bartholomaus, T. C., C. F. Larsen, and S. O'Neel (2013), Does calving matter? Evidence for significant submarine melt, *Earth Planet. Sci. Lett.*, *380*, 21–30.

Bartholomaus, T. C., J. M. Amundson, J. I. Walter, S. O'Neel, M. E. West, and C. F. Larsen (2015), Subglacial discharge at tidewater glaciers revealed by seismic tremor, *Geophys. Res. Lett.*, *42*, 6391–6398, doi:10.1002/2015GL064590.
Bassis, J. N., and S. Jacobs (2013), Diverse calving patterns linked to glacier geometry, *Nat. Geosci.*, *6*(7), 833–836, doi:10.1038/NGEO1887.
Bassis, J. N., and C. C. Walker (2012), Upper and lower limits on the stability of calving glaciers from the yield strength envelope of ice, *Proc. R. Soc. A*, *468*(2140), 913–931, doi:10.1098/rspa.2011.0422.
Battaglia, J., and K. Aki (2003), Location of seismic events and eruptive fissures on the Piton de la Fournaise volcano using seismic amplitudes, *J. Geophys. Res.*, *108*(B8), 2364, doi:10.1029/2002JB002193.
Benn, D. I., N. R. Hulton, and R. H. Mottram (2007), 'Calving laws', 'sliding laws' and the stability of tidewater glaciers, *Ann. Glaciol.*, *46*(1), 123–130, doi:10.3189/172756407782871161.
Bolker, B. M., M. E. Brooks, C. J. Clark, S. W. Geange, J. R. Poulsen, M. H. H. Stevens, and J.-S. S. White (2008), Generalized linear mixed models: A practical guide for ecology and evolution, *Trends Ecol. Evol.*, *24*(3), 127–135, doi:10.1016/j.tree.2008.10.008.
Brown, C. S., M. F. Meier, and A. Post (1982), Calving speed of Alaska tidewater glaciers, with application to Columbia Glacier, *USGS Prof. Pap. 1258-C*, pp. C1–C13, U.S. Gov. Print. Off., Washington, D. C.
Burgess, E. W., R. R. Forster, and C. F. Larsen (2013), Flow velocities of Alaskan glaciers, *Nat. Commun.*, *4*, 2146, doi:10.1038/ncomms3146.
Carr, J., A. Vieli, C. Stokes, S. Jamieson, S. J. Palmer, P. Christoffersen, J. A. Dowdeswell, F. Nick, D. D. Blankenship, and D. A. Young (2015), Basal topographic controls on rapid retreat of Humboldt Glacier, northern Greenland, *J. Glaciol.*, *61*(225), 137–150, doi:10.3189/2015JoG14J128.
Chapuis, A., and T. Tetzlaff (2014), The variability of tidewater-glacier calving: Origin of event-size and interval distributions, *J. Glaciol.*, *60*(222), 622–634, doi:10.3189/2014JoG13J215.
Cook, S., T. Zwinger, I. C. Rutt, S. O. Neel, and T. Murray (2012), Testing the effect of water in crevasses on a physically based calving model, *Ann. Glaciol.*, *53*(60), 90–96, doi:10.3189/2012AoG60A107.
Crawley, M. J. (2009), *The R Book*, 1st ed., 942 pp., John Wiley, West Sussex, England.
Csatho, B. M., A. F. Schenk, C. J. van der Veen, G. Babonis, K. Duncan, S. Rezvanbehbahani, M. R. van den Broeke, S. B. Simonsen, S. Nagarajan, and van Angelen J. H. (2014), Laser altimetry reveals complex pattern of Greenland ice sheet dynamics, *Proc. Natl. Acad. Sci.*, *111*(52), 18,478–18,483, doi:10.1073/pnas.1411680112.
Cuffey, K. M., and W. Paterson (2010), *The Physics of Glaciers*, 4th ed., 693 pp., Elsevier, Boston, Mass.
D'Alessandro, A., and N. A. Ruppert (2012), Evaluation of location performance and magnitude of completeness of the Alaska regional seismic network by the SNES method, *Bull. Seismol. Soc. Am.*, *102*(5), 2098–2115, doi:10.1785/0120110199.
Ekström, G., M. Nettles, and G. A. Abers (2003), Glacial earthquakes, *Science*, *302*(5645), 622–624, doi:10.1126/science.1088057.
Enderlin, E. M., I. M. Howat, and A. Vieli (2013), High sensitivity of tidewater outlet glacier dynamics to shape, *Cryosphere*, *7*(3), 1007–1015, doi:10.5194/tc-7-1007-2013.
Enderlin, E. M., I. M. Howat, S. Jeong, M.-J. Noh, J. H. van Angelen, and M. R. van den Broeke (2014), An improved mass budget for the Greenland ice sheet, *Geophys. Res. Lett.*, *41*, 866–872, doi:10.1002/2013GL059010.
Faillettaz, J., M. Funk, and D. Sornette (2011), Icequakes coupled with surface displacements for predicting glacier break-off, *J. Glaciol.*, *57*(203), 453–460, doi:10.3189/002214311796905668.
Gardner, A. S., et al. (2013), A reconciled estimate of glacier contributions to sea level rise: 2003 to 2009, *Science*, *340*(6134), 852–857.
Glowacki, O., G. B. Deane, M. Moskalik, P. Blondel, J. Tegowski, and M. Blaszczyk (2015), Underwater acoustic signatures of glacier calving, *Geophys. Res. Lett.*, *42*, 804–812, doi:10.1002/2014GL062859.
Gutenberg, B., and C. F. Richter (1944), Frequency of earthquakes in California, *Bull. Seismol. Soc. Am.*, *34*(4), 185–188.
Howat, I. M., J. E. Box, Y. Ahn, A. Herrington, and E. M. McFadden (2010), Seasonal variability in the dynamics of marine-terminating outlet glaciers in Greenland, *J. Glaciol.*, *56*(198), 601–613, doi:10.3189/002214310793146232.
Jenkins, A. (2011), Convection-driven melting near the grounding lines of ice shelves and tidewater glaciers, *J. Phys. Oceanogr.*, *41*(12), 2279–2294.
Johnson, A. J., C. F. Larsen, N. Murphy, A. A. Arendt, and S. L. Zirnheld (2013), Mass balance in the Glacier Bay area of Alaska, U.S.A., and British Columbia, Canada, 1995–2011, using airborne laser altimetry, *J. Glaciol.*, *59*(216), 1995–2011, doi:10.3189/2013JoG12J101.
Jones, G., B. Kulessa, S. Doyle, C. Dow, and A. Hubbard (2013), An automated approach to the location of icequakes using seismic waveform amplitudes, *Ann. Glaciol.*, *54*(64), 1–9, doi:10.3189/2013AoG64A074.
Köhler, A., A. Chapuis, C. Nuth, J. Kohler, and C. Weidle (2012), Autonomous detection of calving-related seismicity at Kronebreen, Svalbard, *Cryosphere*, *6*(2), 393–406, doi:10.5194/tc-6-393-2012.
Krimmel, R. M., and B. H. Vaughn (1987), Columbia Glacier, Alaska: Changes in velocity 1977–1986, *J. Geophys. Res.*, *92*(B9), 8961–8968, doi:10.1029/JB092iB09p08961.
Larsen, C., and M. West (2009), Collaborative research: Relating glacier-generated seismicity to ice motion, basal processes and iceberg calving (Guyot/UAF (AKA Yahtse)), Int. Fed. Digital Seismograph Networks, doi:10.7914/SN/XF_2009.
Larsen, C., E. Burgess, A. Arendt, S. O'Neel, A. Johnson, and C. Kienholz (2015), Surface melt dominates Alaska glacier mass balance, *Geophys. Res. Lett.*, *42*, 5902–5908, doi:10.1002/2015GL064349.
Larsen, C. F., R. J. Motyka, A. A. Arendt, K. A. Echelmeyer, and P. E. Geissler (2007), Glacier changes in southeast Alaska and northwest British Columbia and contribution to sea level rise, *J. Geophys. Res.*, *112*, F01007, doi:10.1029/2006JF000586.
McNabb, R. W., and R. Hock (2014), Alaska tidewater glacier terminus positions, 1948–2012, *J. Geophys. Res. Earth Surf.*, *119*, 153–167, doi:10.1002/2013JF002915.
McNabb, R. W., R. Hock, and M. Huss (2015), Variations in Alaska tidewater glacier frontal ablation, 1985–2013, *J. Geophys. Res. Earth Surf.*, *120*, 120–136, doi:10.1002/2014JF003276.
Montgomery, D. C., E. A. Peck, and G. G. Vining (2001), *Introduction to Linear Regression Analysis*, 3rd ed., 641 pp., John Wiley, New York.
Motyka, R. J. (1997), Deep-water calving at Le Conte Glacier, southeast Alaska, in *Calving Glaciers: Report of a Workshop, Feb. 28–March 2, 1997, Byrd Polar Res. Cent. Rep. No. 15*, edited by C. J. Van der Veen, pp. 115–118, Ohio State Univ., Columbus, Ohio.
Motyka, R. J., and M. Truffer (2007), Hubbard Glacier, Alaska: 2002 closure and outburst of Russell Fjord and postflood conditions at Gilbert Point, *J. Geophys. Res.*, *112*, F02004, doi:10.1029/2006JF000475.
Motyka, R. J., L. Hunter, K. A. Echelmeyer, and C. Connor (2003), Submarine melting at the terminus of a temperate tidewater glacier, LeConte Glacier, Alaska, U.S.A., *Ann. Glaciol.*, *36*(1), 57–65, doi:10.3189/172756403781816374.
Motyka, R. J., W. P. Dryer, J. Amundson, M. Truffer, and M. Fahnestock (2013), Rapid submarine melting driven by subglacial discharge, LeConte Glacier, Alaska, *Geophys. Res. Lett.*, *40*, 5153–5158, doi:10.1002/grl.51011.
Murray, T., et al. (2015), Reverse glacier motion during iceberg calving and the cause of glacial earthquakes, *Science*, *349*(6245), 305–308, doi:10.1126/science.aab0460.

Nettles, M., and G. Ekström (2010), Glacial earthquakes in Greenland and Antarctica, *Annu. Rev. Earth Planet. Sci.*, *38*(1), 467–491, doi:10.1146/annurev-earth-040809-152414.

O'Neel, S., K. A. Echelmeyer, and R. J. Motyka (2003), Short-term variations in calving of a tidewater glacier: LeConte Glacier, Alaska, U.S.A., *J. Glaciol.*, *49*(167), 587–598, doi:10.3189/172756503781830430.

O'Neel, S., W. T. Pfeffer, R. Krimmel, and M. Meier (2005), Evolving force balance at Columbia Glacier, Alaska, during its rapid retreat, *J. Geophys. Res.*, *110*, F03012, doi:10.1029/2005JF000292.

O'Neel, S., H. Marshall, D. McNamara, and W. T. Pfeffer (2007), Seismic detection and analysis of icequakes at Columbia Glacier, Alaska, *J. Geophys. Res.*, *112*, F03S23, doi:10.1029/2006JF000595.

O'Neel, S., C. F. Larsen, N. Rupert, and R. Hansen (2010), Iceberg calving as a primary source of regional-scale glacier-generated seismicity in the St. Elias Mountains, Alaska, *J. Geophys. Res.*, *115*, F04034, doi:10.1029/2009JF001598.

Pettit, E. C., K. M. Lee, J. P. Brann, J. A. Nystuen, P. S. Wilson, and S. O'Neel (2015), Unusually loud ambient noise in tidewater glacier fjords: A signal of ice melt, *Geophys. Res. Lett.*, *42*, 2309–2316, doi:10.1002/2014GL062950.

Press, W. H., B. P. Flannery, S. A. Teukolsky, and W. T. Vetterling (1992), *Numerical Recipes in C. The Art of Scientific Computing*, 2nd ed., 994 pp., Cambridge Univ. Press, New York.

Pritchard, H. D., S. R. M. Ligtenberg, H. a. Fricker, D. G. Vaughan, M. R. van den Broeke, and L. Padman (2012), Antarctic ice-sheet loss driven by basal melting of ice shelves, *Nature*, *484*(7395), 502–505, doi:10.1038/nature10968.

Qamar, A. (1988), Calving icebergs: A source of low-frequency seismic signals from Columbia Glacier, Alaska, *J. Geophys. Res.*, *93*(B6), 6615–6623.

Reyes, C. G., and M. E. West (2011), The waveform suite: A robust platform for manipulating waveforms in MATLAB, *Seismol. Res. Lett.*, *82*(1), 104–110, doi:10.1785/gssrl.

Richardson, J., G. Waite, K. FitzGerald, and W. Pennington (2010), Characteristics of seismic and acoustic signals produced by calving, Bering Glacier, Alaska, *Geophys. Res. Lett.*, *37*, L03503, doi:10.1029/2009GL041113.

Rignot, E., I. Velicogna, M. R. van den Broeke, A. Monaghan, and J. Lenaerts (2011), Acceleration of the contribution of the Greenland and Antarctic ice sheets to sea level rise, *Geophys. Res. Lett.*, *38*, L05503, doi:10.1029/2011GL046583.

Rignot, E., J. Mouginot, C. F. Larsen, Y. Gim, and D. Kirchner (2013a), Low-frequency radar sounding of temperate ice masses in Southern Alaska, *Geophys. Res. Lett.*, *40*, 5399–5405, doi:10.1002/2013GL057452.

Rignot, E., J. Mouginot, C. F. Larsen, Y. Gim, and D. Kirchner (2013b), *IceBridge WISE L2 Geolocated Ice Thickness and Surface Elevation*, Natl. Snow and Ice Data Cent., Boulder, Colo.

Ritchie, J. B., C. S. Lingle, R. J. Motyka, and M. Truffer (2008), Seasonal fluctuations in the advance of a tidewater glacier and potential causes: Hubbard Glacier, Alaska, U.S.A., *J. Glaciol.*, *54*(186), 401–411.

Schild, K. M., and G. S. Hamilton (2013), Seasonal variations of outlet glacier terminus position in Greenland, *J. Glaciol.*, *59*(216), 759–770, doi:10.3189/2013JoG12J238.

Sciascia, R., F. Straneo, C. Cenedese, and P. Heimbach (2013), Seasonal variability of submarine melt rate and circulation in an East Greenland fjord, *J. Geophys. Res. Oceans*, *118*, 2492–2506, doi:10.1002/jgrc.20142.

Stearns, L. A., G. S. Hamilton, C. J. van der Veen, D. C. Finnegan, S. O. Neel, J. B. Scheick, and D. E. Lawson (2015), Glaciological and marine geological controls on terminus dynamics of Hubbard Glacier, southeast Alaska, *J. Geophys. Res. Earth Surf.*, *120*, 1065–1081, doi:10.1002/2014JF003341.

Stein, S., and M. Wysession (2003), *An Introduction to Seismology, Earthquakes, and Earth Structure*, 498 pp., Blackwell Publ., Malden, Mass.

Sutherland, D. A., and F. Straneo (2012), Estimating ocean heat transports and submarine melt rates in Sermilik Fjord, Greenland, using lowered acoustic Doppler current profiler (LADCP) velocity profiles, *Ann. Glaciol.*, *53*(60), 50–58, doi:10.3189/2012AoG60A050.

Truscott, T. T., and A. H. Techet (2009), Water entry of spinning spheres, *J. Fluid Mech.*, *625*, 135–163, doi:10.1017/S0022112008005533.

Tsai, V., and G. Ekström (2007), Analysis of glacial earthquakes, *J. Geophys. Res.*, *112*, F03S22, doi:10.1029/2006JF000596.

Tsai, V., J. Rice, and M. Fahnestock (2008), Possible mechanisms for glacial earthquakes, *J. Geophys. Res.*, *113*, F03014, doi:10.1029/2007JF000944.

van der Veen, C. J. (2002), Calving glaciers, *Prog. Phys. Geog.*, *26*(1), 96–122, doi:10.1191/0309133302pp327ra.

Veitch, S. A., and M. Nettles (2012), Spatial and temporal variations in Greenland glacial-earthquake activity, 1993–2010, *J. Geophys. Res.*, *117*, F04007, doi:10.1029/2012JF002412.

Walter, F., J. M. Amundson, S. O'Neel, M. Truffer, M. Fahnestock, and H. A. Fricker (2012), Analysis of low-frequency seismic signals generated during a multiple-iceberg calving event at Jakobshavn Isbræ, Greenland, *J. Geophys. Res.*, *117*, F01036, doi:10.1029/2011JF002132.

Warren, C. R., N. F. Glasser, S. Harrison, V. Winchester, A. R. Kerr, and A. Rivera (1995), Characteristics of tide-water calving at Glaciar San Rafael, Chile, *J. Glaciol.*, *41*(138), 273–289.

West, M., C. Larsen, M. Truffer, S. O'Neel, and L. LeBlanc (2010), Glacier microseismicity, *Geology*, *38*(4), 319–322, doi:10.1130/G30606.1.

Wolf, L. W., and J. N. Davies (1986), Glacier-generated earthquakes from Prince William Sound, Alaska, *Bull. Seismol. Soc. Am.*, *76*(2), 367–379.

Xu, Y., E. Rignot, D. Menemenlis, and M. Koppes (2012), Numerical experiments on subaqueous melting of Greenland tidewater glaciers in response to ocean warming and enhanced subglacial discharge, *Ann. Glaciol.*, *53*(60), 229–234, doi:10.3189/2012AoG60A139.

Zimmer, V. L., B. D. Collins, G. M. Stock, and N. Sitar (2012), Rock fall dynamics and deposition: An integrated analysis of the 2009 Ahwiyah Point rock fall, Yosemite National Park, U.S.A., *Earth Surf. Processes Landforms*, *37*(6), 680–691, doi:10.1002/esp.3206.